Paper No.
4299

CORROSION 2014
Collaborate. Educate. Innovate. Mitigate.
March 9-13, 2014 • Henry B. Gonzalez Convention Center • San Antonio, Texas, U.S.A.

Impact of Oxygen Ingress in CO_2 Corrosion of Mild Steel

Nor Roslina Rosli, Yoon-Seok Choi, David Young
Institute for Corrosion and Multiphase Technology,
Department of Chemical and Biomolecular Engineering, Ohio University
342 West State Street
Athens, OH 45701
USA

ABSTRACT

The development of carbon capture and storage (CCS) technologies have helped facilitate the success of CO_2-EOR injection operations. However, captured CO_2 from anthropogenic sources can potentially contain oxygen which will increase the risk of corrosion. A preliminary study was conducted at 1 bar to investigate the effect of oxygen ingress on the iron carbonate ($FeCO_3$) corrosion product layers generated during CO_2 corrosion of mild steel. Carbon steel (UNS G10180) samples were immersed in a CO_2-saturated 1 wt.% NaCl electrolyte for 7 days, with the tests being perturbed with 1 ppm O_2 at different experimental times. Iron carbonate film-forming conditions (80°C and pH 6.6 ± 0.1) were maintained throughout experiments. Electrochemical measurements indicated a decrease in corrosion rate due to scale formation that conferred some degree of protection to the steel surface. Although the corrosion rates at the conclusion of all tests were relatively low, localized corrosion was observed. Surface analysis showed severe corrosion and confirmed the formation of iron (III) oxides and iron carbonate. A distinct feature of oxygen ingress is the formation of tubercles on the steel surfaces. The degradation of initially formed iron carbonate occurred concurrently with the development of localized corrosion features as deep as 100 µm. It can be concluded that oxygen ingress, even at low concentrations, can have a profound effect on sweet corrosion of mild steel.

Key words: Oxygen, CO_2 corrosion, mild steel, iron oxide

INTRODUCTION

Since the 1940s, an increasing number of oil reservoirs around the world have been abandoned upon their depletion. Injection of carbon dioxide (CO_2) into oil wells in such fields has the potential to significantly extend their life by enabling feasible economic recovery of the remaining trapped oil. This technology is referred to as CO_2 Enhanced Oil Recovery (CO_2-EOR).

Carbon dioxide, in combination with any aqueous phase, can cause damage and failure to carbon steel, the most widely used infrastructure material in the oil and gas industry[1]; this phenomenon is termed CO_2 corrosion, also known as 'sweet corrosion'. Development of Carbon Capture and Storage (CCS) technologies has the potential to supply CO_2 from anthropogenic sources to CO_2-EOR operations. However, captured CO_2 is impure and can potentially contain oxygen (O_2), which poses a higher risk of corrosion.[2]Corrosion rate increases proportionally with increasing dissolved oxygen concentration.[3, 4] High concentrations of O_2 lead to formation of iron oxides as it oxidizes ferrous ions into ferric ions, preventing the formation of protective iron carbonate ($FeCO_3$) layers; thus increasing the corrosion rate of carbon steel. A review of the types and concentrations of impurities in CO_2 derived from a range of capture technologies indicated that the O_2 concentration in a CO_2 stream from the oxyfuel process can approach 3 vol.%, this has the potential to lead to severe corrosion of steel tubulars.[5-7] Techniques to eliminate impurities in the CO_2 gas are available. However, this can be uneconomic. Therefore, it is more feasible to transport and inject impure CO_2 directly for geologic sequestration.[8]

Extensive studies have been conducted on CO_2 corrosion and O_2 corrosion independently of each other. However, there is minimal literature on corrosion in mixed CO_2-O_2 environments. This necessitates study of the impact of trace concentrations of oxygen in anthropogenic CO_2 on the integrity of carbon steel and its impact on iron carbonate corrosion products. Iron carbonate has limited stability in the presence of oxygen, due to the oxidation of Fe(II) to Fe(III). An objective of this study was to investigate the stability of iron carbonate on a mild steel surface with simulated ingress of O_2 at atmospheric pressure conditions as a prelude to conducting experiments that simulate high pressure environments.

EXPERIMENTAL PROCEDURE

UNS G10180 steel specimens were used in this study for electrochemical measurements, surface analysis, and weight loss measurements. Prior to being immersed in the test solution, the specimens were polished with up to 600-grit silicon carbide (SiC) paper, rinsed and cleaned with isopropyl alcohol in an ultrasonic bath, and dried.

A glass cell apparatus, as shown in Figure 1, was utilized to conduct all the low-pressure corrosion tests described in this study. The glass cell lid is fabricated with slots for a pH electrode, a thermocouple, gas inlet and outlet, reference electrode, working electrode, counter electrode, and weight loss samples. The glass cell was filled with 2 liters of 1 wt.% NaCl solution as the electrolyte. Prior to each experiment carbon dioxide or a carbon dioxide and oxygen mixture was bubbled through this solution for about 1 hour until the desired stable concentration of oxygen is achieved. Oxygen concentration in the water phase was monitored using an Orbisphere 410[†] oxygen meter. A pure carbon dioxide saturated solution showed a reading of below 10 ppb of oxygen in the gas phase (25°C), versus 3 ppm oxygen in the mixed gas system at standard temperature and pressure. Gas was continuously bubbled for the duration of the tests. The total pressure of the glass cell was 1 bar. The desired temperature was maintained using a hotplate, controlled with a thermocouple immersed into the solution. Once the solution temperature stabilized, its pH was adjusted by adding deoxygenated reagent grade $NaHCO_3$ or HCl. Deoxygenated ferrous chloride ($FeCl_2 \cdot 4H_2O$) solution was added to provide additional Fe^{2+} to achieve a high initial $FeCO_3$ saturation value, in order to accelerate the formation of the protective $FeCO_3$ layer. The test matrix is shown in Table 1.

[†] Trade name

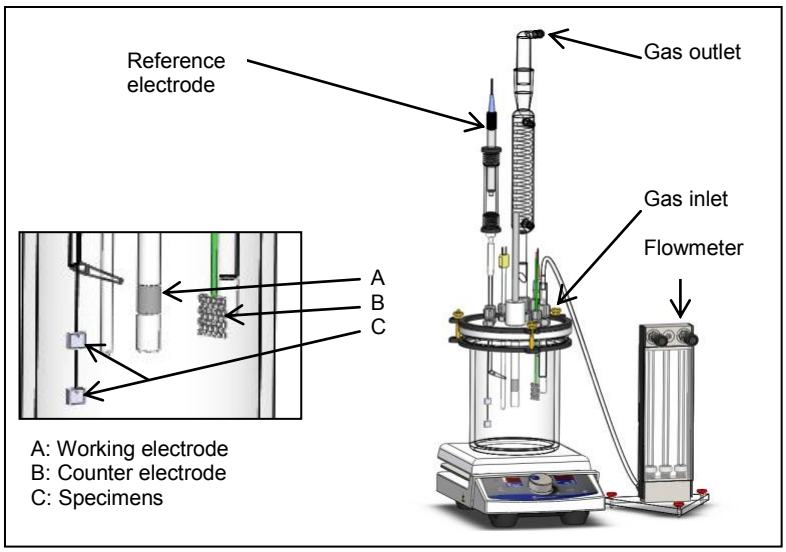

Figure 1: Glass cell Set-up

Table 1
Test matrix for corrosion testing.

	Test conditions
Temperature	80°C
Initial pH	6.6
Total Pressure	1 bar
O_2 Concentration	1 ppm in liquid phase
Electrolyte	1 wt.% NaCl
Initial Fe^{2+} Concentration	50 ppm
Initial $FeCO_3$ Saturation	277
Duration	7 days
Flow Rate	Stagnant

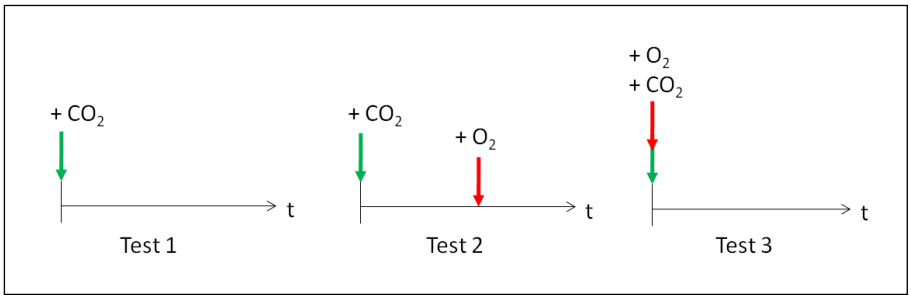

Figure 2: Three different tests for corrosion product formation experiments.

In the present study, the corrosion experiments were conducted with three different procedures, labeled as follows, and illustrated schematically in Figure 2:

a) Test 1: Baseline CO_2 experiment.
b) Test 2: O_2 introduced after 2 days of iron carbonate formation. This was done to determine the effect of oxygen ingress on the iron carbonate layer that is already on the steel surface.
c) Test 3: O_2 introduced from the beginning of the experiment. This study was conducted to investigate the effect of oxygen ingress on bare steel.

At the end of experiments, the test specimens were promptly removed from the electrolyte, rinsed with isopropyl alcohol and dried to prevent the onset of further corrosion processes. The test specimens were then analyzed using scanning electron microscopy (SEM), energy dispersive X-ray spectroscopy (EDS), X-ray diffraction (XRD) and Raman spectroscopy.

Sample specimens from each experiment were also treated with Clarke solution (ASTM G1-03)[(1)] to completely remove all corrosion products, in order to determine the weight loss of the material resulting from the test exposure and subsequent calculation of corrosion rate. Weight loss from the specimens in all tests was recorded and translated into corrosion rate using the following formula:

$$CR = \frac{W}{DAT} \tag{1}$$

Where W is weight loss in grams, D is density of the steel specimen in g/cm^3, A is the area of the specimen in cm^3, and T is experimental time in seconds. The corrosion rate in cm/s was converted into units of mm/y with appropriate unit conversion. Treated specimens were also characterized by profilometry, using an infinite focus microscope (IFM), to determine the surface profile of the corroded steel surface and measure penetration rate relating to any observable pitting attack.

RESULTS

ELECTROCHEMICAL MEASUREMENTS

Development of iron carbonate layers leads to a single order of magnitude decrease in the general corrosion rate over the first three hours for all three experiments, as shown in Figure 3. In a pure CO_2 baseline experiment, Test 1, the corrosion rate kept on decreasing monotonously until the end of the experiment, to *ca.* 0.1 mm/y, as the protective $FeCO_3$ layer develops. Introduction of 3 ppm oxygen on the second day, Test 2, showed similar behavior of decreasing corrosion rate; however, there was a greater scatter in corrosion rate values after addition of oxygen. In the test where 3 ppm oxygen was made available from the very beginning of the experiment, Test 3, the corrosion rate decreased rapidly for the first few hours and then increased and remained high for three days. After 7 days, the corrosion rate of the three tests eventually decreased to values less than 0.2 mm/y. This shows that the corrosion product was able to provide some protection to the steel surface even in the presence of oxygen. The values of corrosion rates obtained from LPR were integrated to obtain the time-averaged corrosion rate values, as shown in Table 2.

The corrosion potential, E_{corr}, was monitored throughout the tests as illustrated in Figure 4. There was an immediate shift in potential as oxygen was added to the system in Test 2. Investigation of the corrosion rate in Test 3 showed that the corrosion rate started to decrease to about 0.3 ± 0.2 mm/y concurrent with an abrupt shift in the open-circuit potential (OCP) to a more positive value, from *ca.* −690 ± 0.1 mV to *ca.* −475 ± 25 mV.

The overall variation in the pH values throughout the experiments was insignificant, as shown in Figure 5. This is a good indication that the production and consumption of hydrogen ions due to water chemistry (H_2CO_3 formation and dissociation) and CO_2 corrosion was balanced by the production of hydroxyl ions. The total iron concentration in the electrolyte, which was determined daily *via* spectrophotometry, is plotted in Figure 6.

[(1)] American Society for Testing and Materials (ASTM), 100 Barr Harbor Drive, PO Box C700, West Conshohocken, PA, 19428-2959

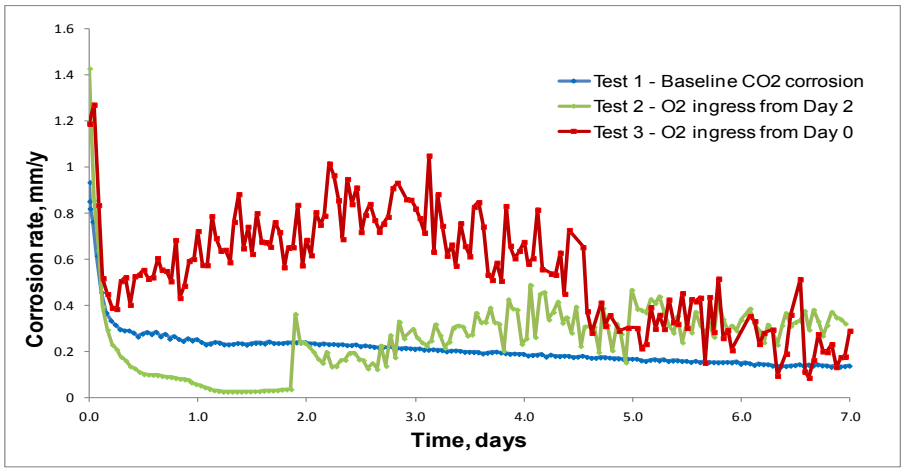

Figure 3: Corrosion rates at three different test conditions using LPR (*B* = 26 mV)

Table 2
Time-averaged corrosion rates integrated from LPR results.

Experiment	Time-averaged corrosion rate from LPR, mm/y	Standard deviation
Test 1	0.25	0.16
Test 2	0.21	0.11
Test 3	0.56	0.23

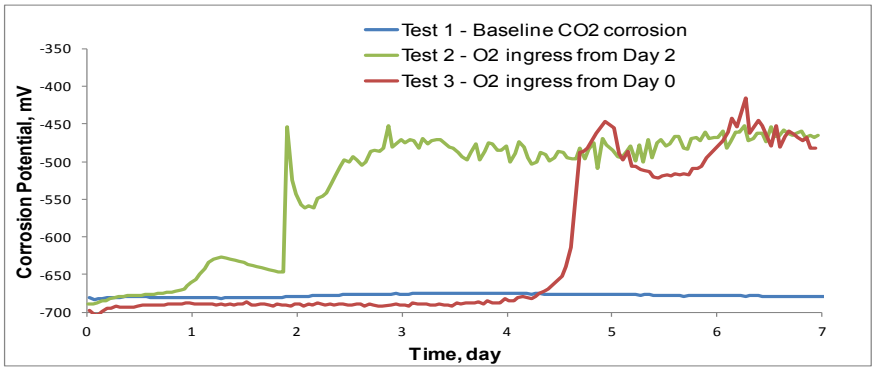

Figure 4: Variation in the corrosion potential measured by a potentiostat.

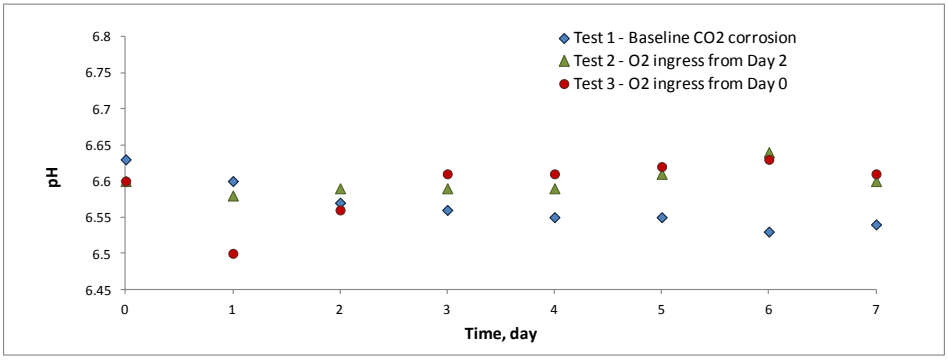

Figure 5: Bulk pH of test solutions.

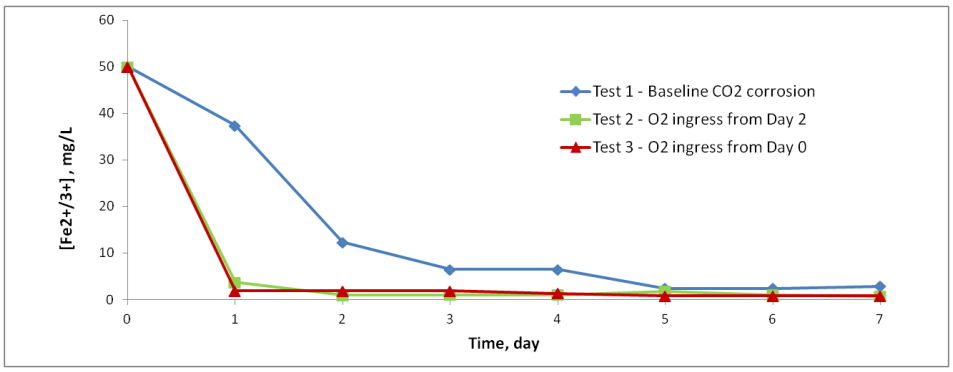

Figure 6: Total aqueous iron concentration data.

SURFACE ANALYSIS

The top view of the corrosion product scale on the specimens from the three tests shows that the nature of the iron carbonate differs in terms of coverage and morphology.

Test 1: Baseline CO_2 Corrosion

The steel surface was densely coated with prismatic iron carbonate crystals in the CO_2 baseline test (Test 1), as shown in Figure 7. Removal of the corrosion product by Clarke solution treatment reveals a surface that shows general corrosion over the entire steel surface with no signs of pitting. Polishing marks were still fairly visible on the steel surface, as shown in Figure 8.

.

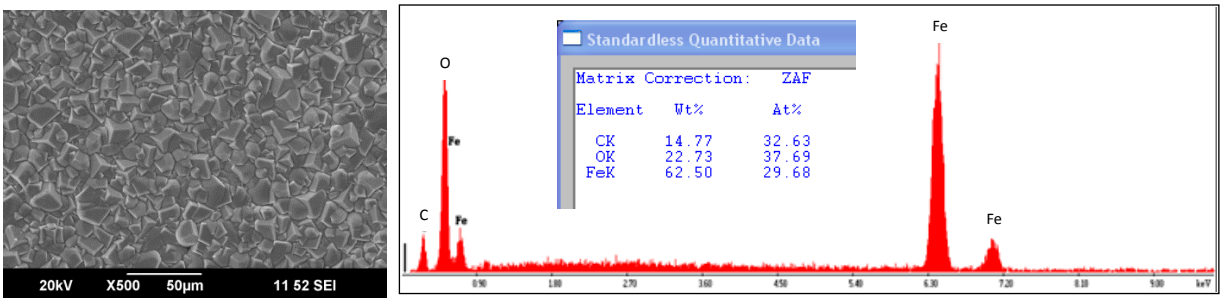

Figure 7: SEM image and EDS spectra of sample for Test 1

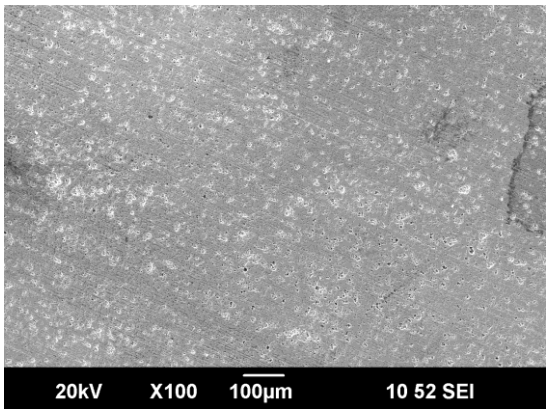

Figure 8: SEM image of steel surface for Test 1 after corrosion product removal

Test 2: O_2 ingress on Day 2

The steel surface generated after ingress of oxygen after 2 days shows development of clusters of small globular-shaped pseudo-cubic crystals deposited on top of the prismatic iron carbonate crystals. These clusters of crystals tend to accumulate and form mounds and craters as demonstrated in Figure 9. The EDS analysis, Figure 10, of the smaller pseudo-cubic crystals showed a higher intensity O peak and lower intensity carbon C peak, compared to the EDS analysis of the larger prismatic crystals, which gives a good indication of the presence of iron oxide. Nevertheless, this result is questionable due to the thin and porous structure of iron oxide.

The formation of $FeCO_3$ in the first two days of the test provided some protection to the steel surface, hence the drop in the corrosion rate as demonstrated in the electrochemical measurements. The $FeCO_3$ layer was then perturbed by iron oxide formation on Day 2, which caused the increase in the general corrosion rate after oxygen was introduced to the system. By the end of the test on Day 7, the accumulation of corrosion product provided some form of protection to the steel surface as demonstrated by the decrease in corrosion rate.

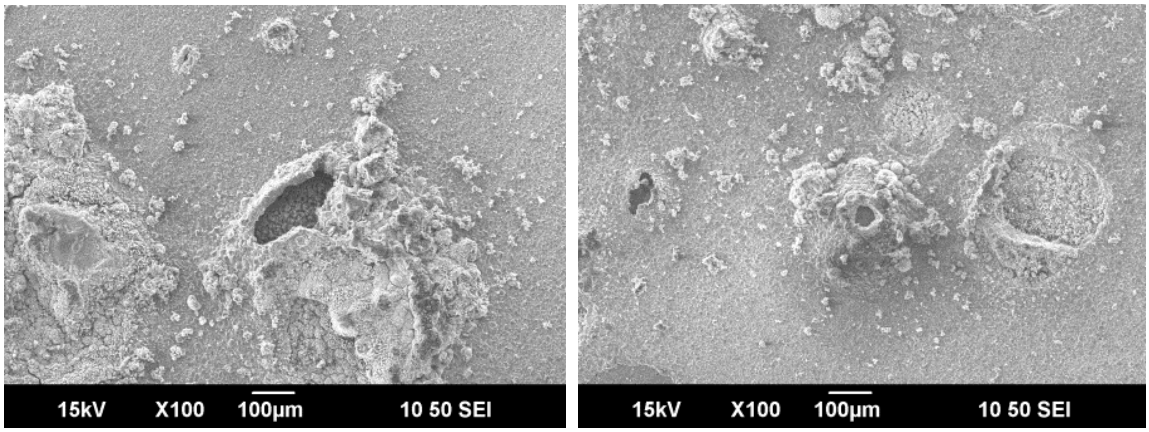

Figure 9: SEM image of oxide clusters on $FeCO_3$ layer in Test 2

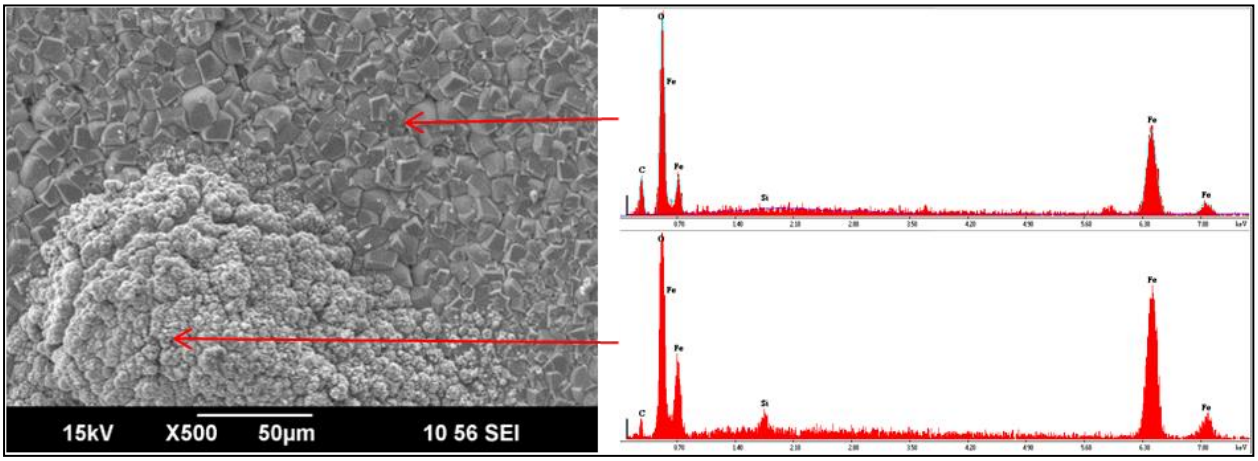

Figure 10: SEM image and EDS spectra of sample in Test 2

The cross-sectional view of the corrosion product on the steel surface demonstrates a dome-like hollow tubercular structure. The different shades of grey shown in the SEM backscatter image in Figure 11 are

indicative of compositional variation in the corrosion product layer. Heavy elements scatter electrons more effectively than light elements. Therefore, there is a correlation between the atomic numbers of the elements present and the contrasting shades of grey observed in SEM images.[9, 10] The epoxy that was used to impregnate the specimen appeared black on the image due to the lesser amount of backscattered electrons from a surface constituted from light elements (C, H, O). The steel, consisting overwhelmingly of Fe, is a light grey. Iron oxide and carbonate corrosion products are of intermediate shading.

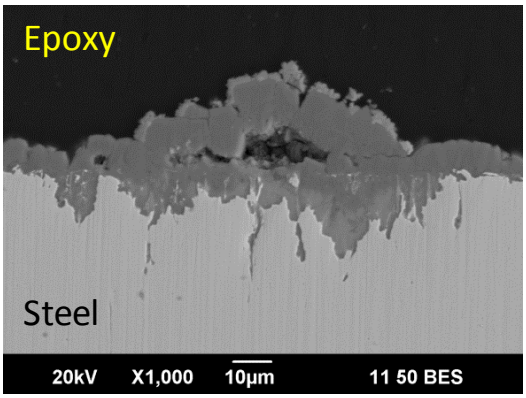

Figure 11: Cross-sectional view of the sample from Test 2

Figure 12 shows the steel surface of the specimens after Clarke solution treatment. It is apparent that iron oxide was able to partially remove and penetrate through the formed iron carbonate, leading to damage of the steel surface. The attack was observed in the form of wide localized corrosion features.

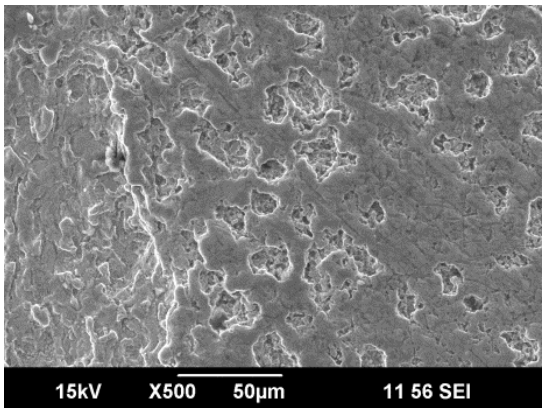

Figure 12: SEM image of the steel surface from Test 2 after corrosion product removal

The pit depth and surface profile was investigated using an infinite focus microscope (IFM) profilometer, as shown in Figure 13. The maximum pit depth found was 100 µm, which corresponds to a penetration rate of 4.6 mm/y. Visual inspection of the pits shows wide widths. False color images were also produced to help distinguish the subtle variations by expanding the range of visible hues, see Figure 13.

One method to determine the severity of localized corrosion is by measuring its pitting factor, which is the ratio of the pit penetration to the average penetration obtained from weight loss of the metal. A pitting factor of 1 suggests uniform corrosion while higher values suggest localized corrosion. With the resulting corrosion rate from weight loss calculation (1.31 mm/y), the pitting factor of this test was found to be 3.4. This would be consistent with low severity localized corrosion.

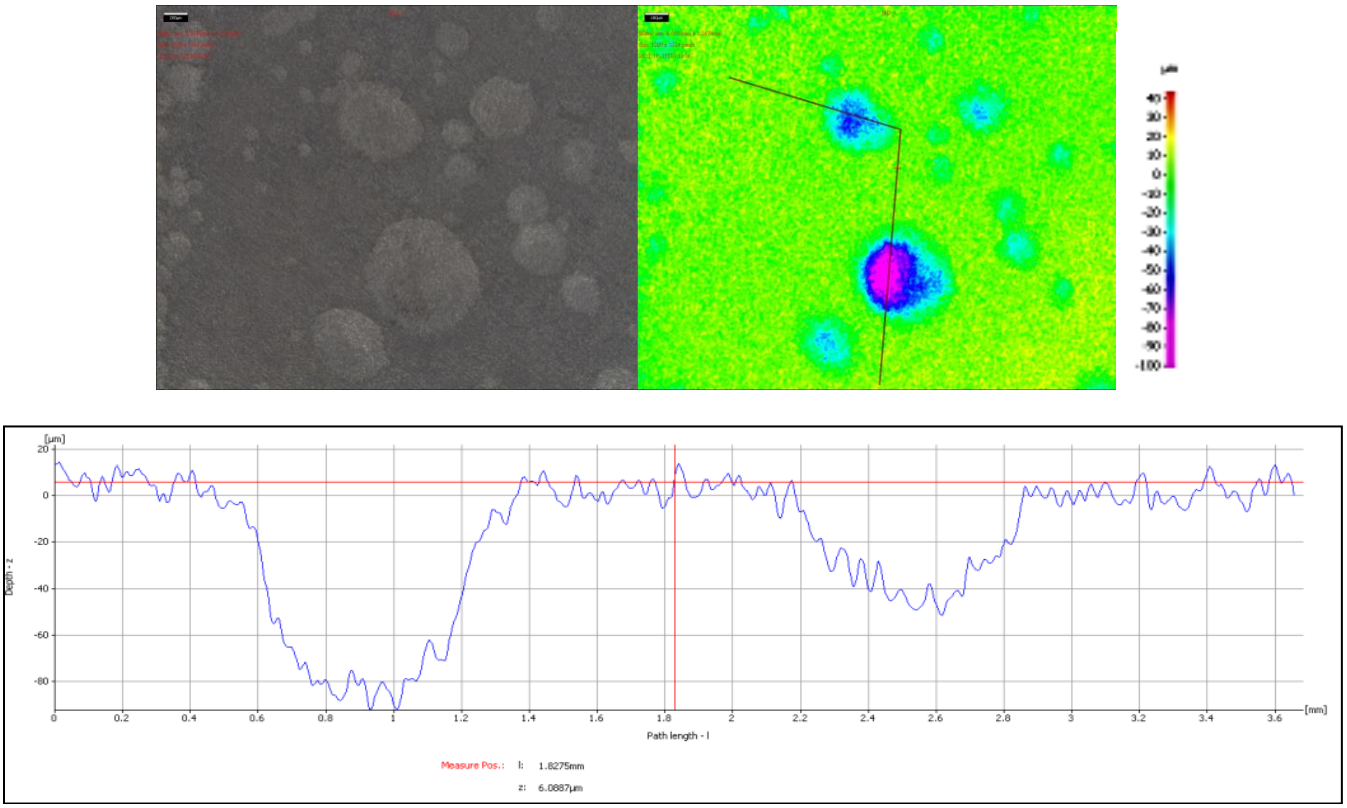

Figure 13: Surface profile of pits on specimen from Test 2.

Test 3: O_2 ingress from Day 0

Although oxygen was continuously bubbled into the solution throughout the duration of the experiment corresponding to Test 3 and maintained at 1 ppm, some $FeCO_3$ was still able to form on the steel surface. However, the presence of oxygen had a significant impact on the nature of $FeCO_3$ formation on the steel surface, which was not fully covered by $FeCO_3$ prismatic crystals as is shown in Figure 14. The surface was instead covered by a combination of prismatic and smaller sized crystals. EDS spectra provides a good indication of the presence of iron oxides on the steel surface. The iron oxide crystals obstructed the formation of iron carbonate and resulted in partial coverage by iron carbonate of the steel surface. The attack by oxygen was more rapid than the formation of $FeCO_3$ as a corrosion product. The previously noted clustering and cratering effects were also observed in Test 3.

Further investigation of the corrosion product layer shows the obstructive nature of iron oxide towards iron carbonate crystals. The $FeCO_3$ prisms also appeared imperfectly formed, as illustrated in Figure 15. When oxygen was introduced from the beginning of the experiment iron oxides, such as Fe_2O_3 and Fe_3O_4, were hypothesized to grow simultaneously with $FeCO_3$ resulting in mixed crystal constituents within the corrosion product layer.

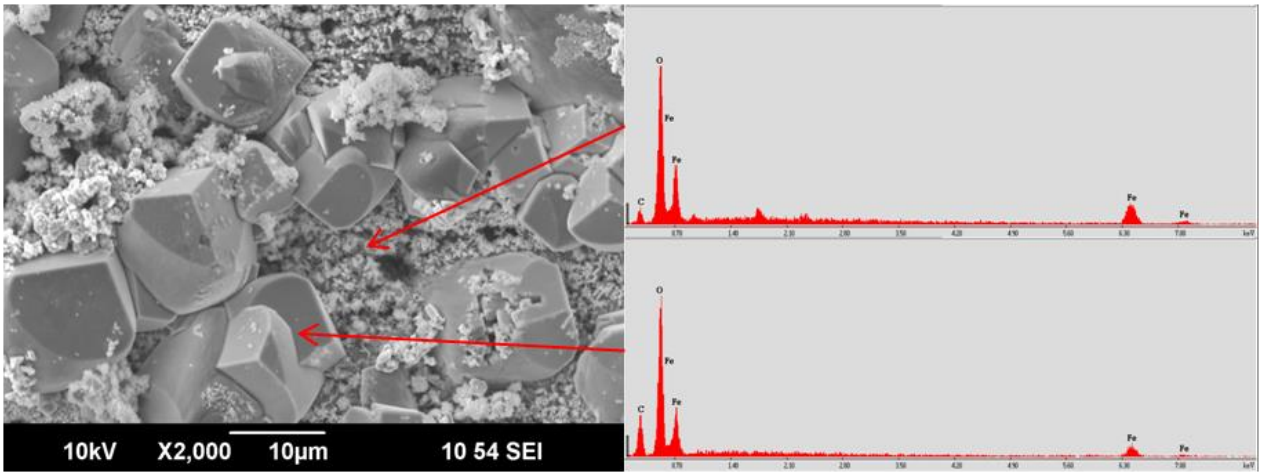

Figure 14: SEM image and EDS spectra of sample in Test 3

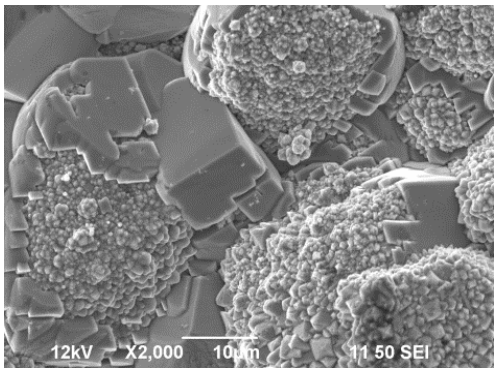

Figure 15: Imperfectly formed iron carbonate crystals with iron oxide.

A cross-sectional view of the specimen was observed with SEM using back-scattered electrons to provide information on the compositional difference of the corrosion product layer, as shown in Figure 16. The contrasting shades produced by the SEM backscattered image for the cross-sectional view shows formation of a corrosion product tubercle on top of a wide localized pit.

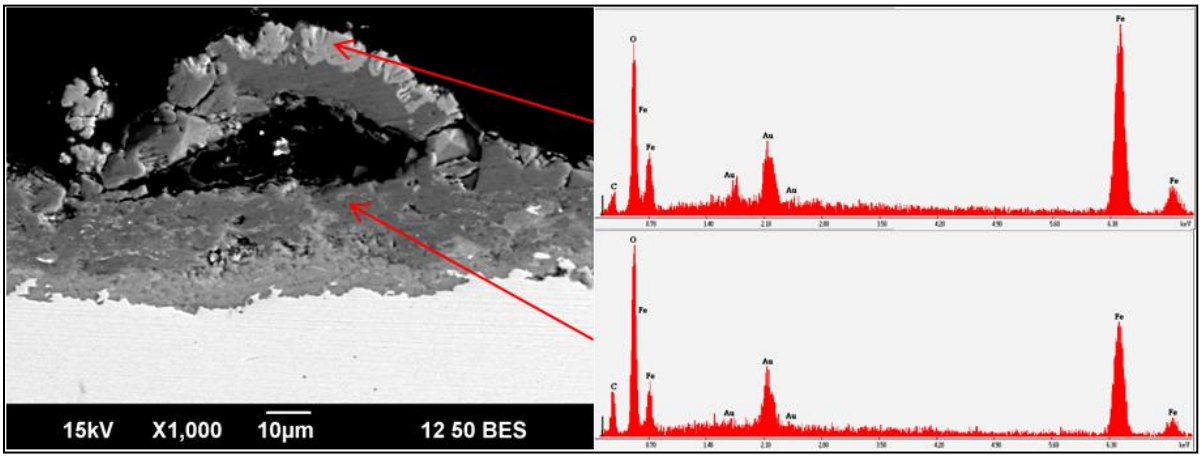

Figure 16: SEM image and EDS spectra of Test 3 sample surface cross-section

The composition of the tubercle is in agreement with tubercle models suggested by previous corrosion researchers.[11-16] Tubercles commonly consist of five structural features; an outer crust (Fe_2O_3,

hematite), inner shell (Fe_3O_4, magnetite), core ($FeCO_3$, siderite & $Fe(OH)_2$, ferrous hydroxide), fluid cavity and steel floor.[13] The fluid filled cavity can be seen here as a black region that has been filled by epoxy. The lighter colored region at the top of the tubercle can be speculated to be magnetite, with EDS analyses showing a low intensity C peak. Smaller particles on the outermost region of the tubercle were too porous to be meaningfully analyzed by EDS since they are filled with carbon-containing epoxy. Both specimens at Test 2 and Test 3 showed similar tubercle characteristics.

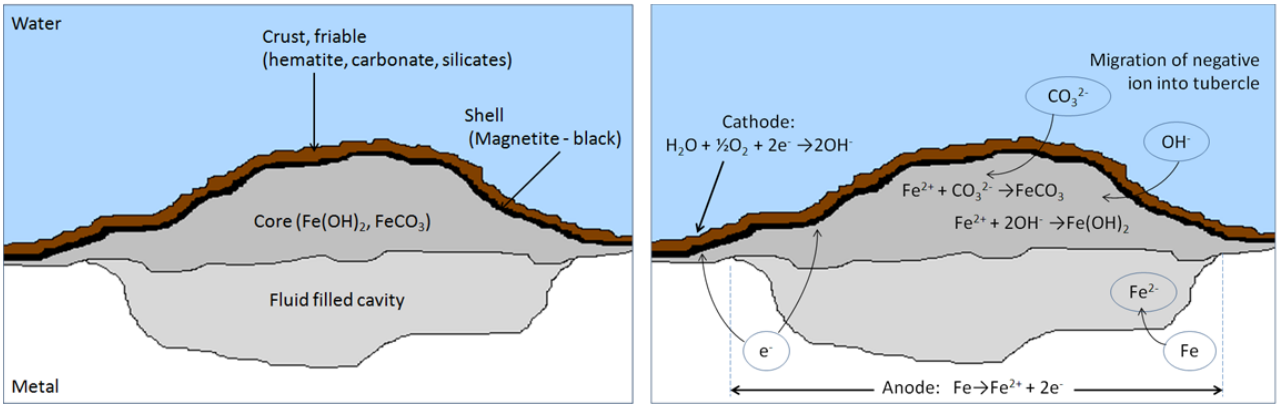

Figure 17: Schematic diagram of a tubercle based on a study described by Herro.[13]

Tuberculation is caused by localized electrochemical processes at distinguishable anodic and cathodic sites. Localized regions of metal loss are capped with accumulated corrosion products and deposits of precipitates. An oxygen deficient region below the tubercle creates an anodic site where dissolution of metal results in accumulation of ferrous and ferric ions. Cathodic sites are created around the surrounding area of the tubercle, increasing the pH, and causing a decrease in the solubility of carbonate and other precipitates.[13]

The ingress of 3 ppm oxygen in the bulk solution at Test 3 caused more severe damage to the entire steel surface. This was observed when the corrosion product was chemically removed from the steel surface. Polish marks could no longer be seen on the surface of this specimen, as shown in Figure 18.

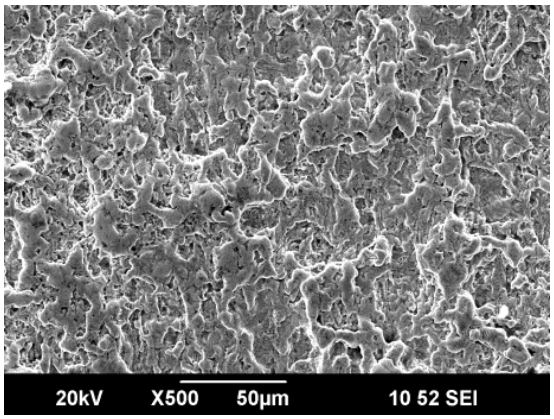

Figure 18: SEM image of steel surface for Test 3 after corrosion product removal

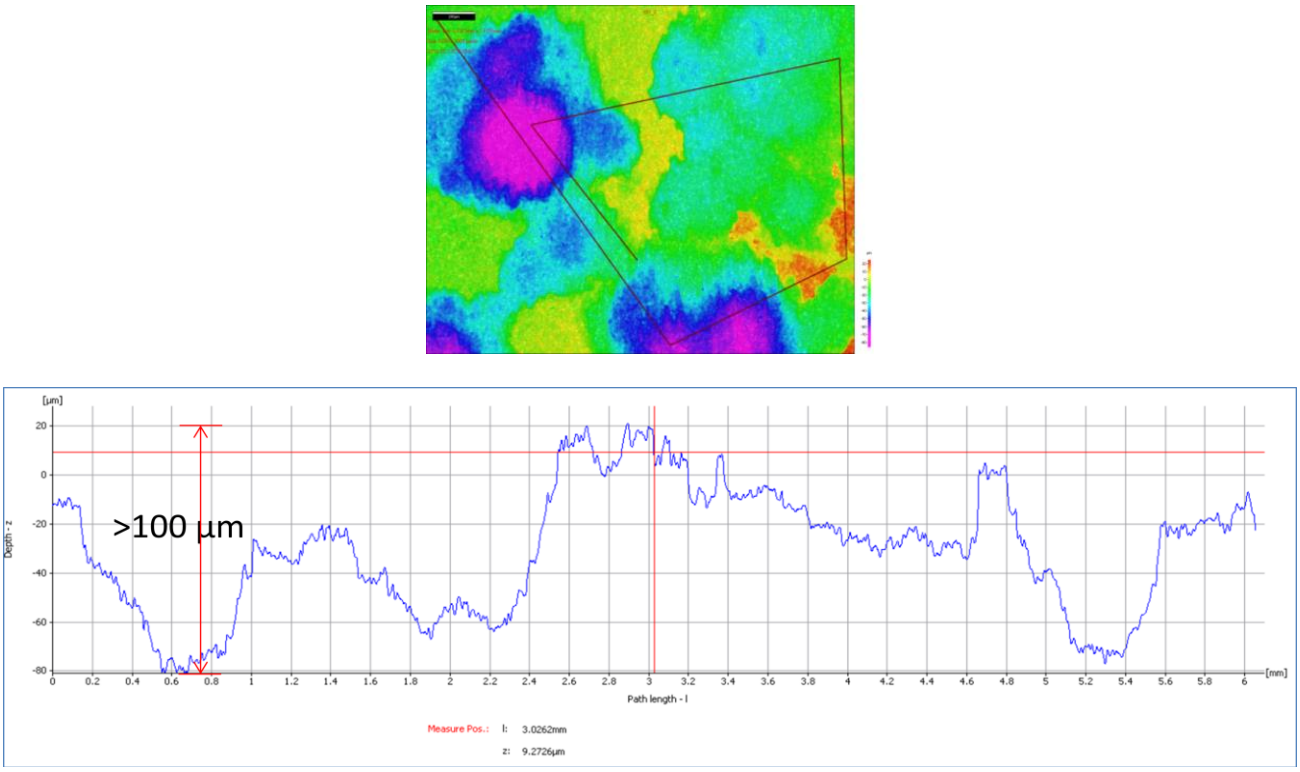

Figure 19: Pit depth analysis of specimen for Test 3.

Although the surface profile from IFM analysis showed pits *ca.*100 µm deep, as shown in Figure 19, it does not give an accurate depth of the etched surface from the original steel surface because the whole surface was severely damaged.

Results from weight loss measurement.

Specimens that were subjected to oxygenated environments (Test 2 and 3) experienced a higher weight loss compared to the specimen that was not subjected to O_2 exposure. The corresponding corrosion rates of the specimens in Test 2 and Test 3 were one order of magnitude greater than for Test 1. Electrochemical measurements for Tests 2 and 3 showed higher corrosion rates determined *in situ* throughout the period of the tests and supports the findings from the weight loss calculations.

Table 3
Summarized corrosion rates of all tests calculated from weight loss measurement.

Experiment	Corrosion Rate *via* Weight Loss, mm/y
Test 1	0.10
Test 2	1.31
Test 3	1.07

X-Ray Diffraction and Raman Spectroscopy

Elemental analyses using EDS provide an initial determination of the chemical compositions of the corrosion product; however, it is inconclusive since it does not identify the exact identity, or identities, of the phases present. Although the identity of the chemical compounds can be deduced based on the measured atomic ratios, this can be misinterpreted – particularly if more than one phase is present or if

polymorphism is possible. X-ray diffraction (XRD) and Raman spectroscopy are then utilized to confirm the presence, or absence, of particular phases.

Figure 20 and Figure 21 correspond to the XRD patterns of specimens removed at the end of the experiments corresponding to Test 2 and Test 3. The analyses revealed a pattern characteristic of siderite ($FeCO_3$) as the main component in the corrosion product layer of the recovered specimen for Test 2, while hematite (Fe_2O_3) and magnetite (Fe_3O_4) were detected as the main components in Test 3. Substrate α-Fe peaks were notably absent, consistent with formation of a thick corrosion product layer.

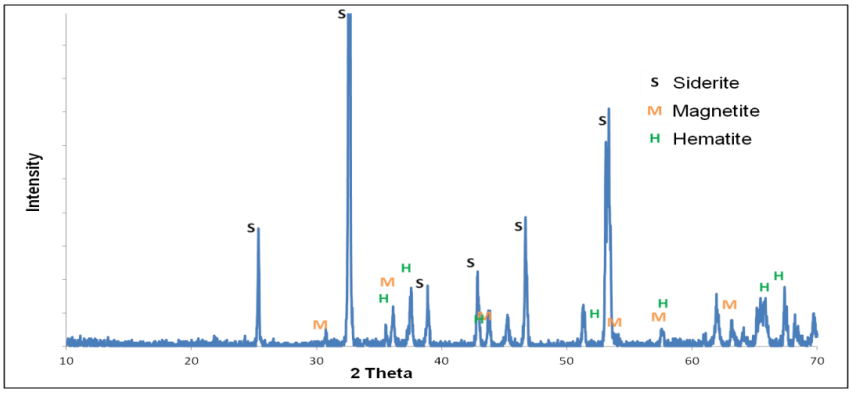

Figure 20: X-ray diffraction of the specimen for Test 2.

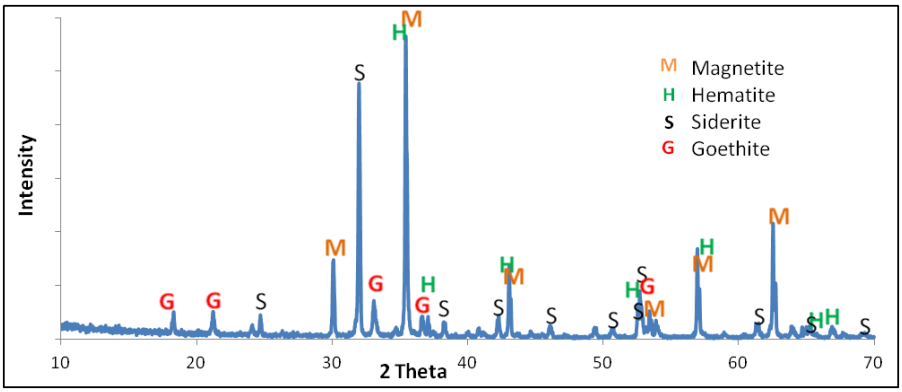

Figure 21: X-ray diffraction of the specimen for Test 3.

Raman spectroscopy is another method that was utilized to complement the XRD data. Peaks for hematite, magnetite, goethite and siderite were identified, as shown in Figure 22. Note the absence of a strong vibrational mode at *ca.* 1100 cm^{-1}, which is diagnostic for the presence of carbonate (CO_3^{2-}). Taken in conjunction with the XRD data, the collected Raman data would be consistent with the presence of a primarily hematite-type ferric oxide (Fe_2O_3) overlying the formed iron carbonate ($FeCO_3$).

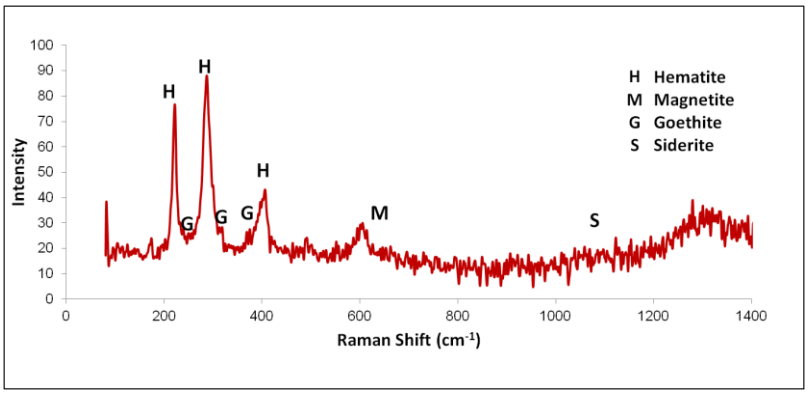

Figure 22: Raman spectra of specimen from Test 3.

CONCLUSIONS

The above described tests provide a basis for comparison with future studies simulating oxygen ingress in sweet corrosion environments at high pressure field conditions. The observed influence of oxygen on sweet corrosion at low pressure is profound and must be seriously considered when performing corrosion control of mild steel. Localized corrosion was observed although the corrosion rates at the conclusion of all tests were relatively low. Surface analysis showed degradation of iron carbonate crystals and formation of iron oxides. This degradation of initially formed iron carbonate occurred concurrently with the development of localized corrosion features as deep as 100 µm. XRD and Raman confirm the formation of magnetite (Fe_3O_4), hematite (α-Fe_2O_3), and goethite (α-FeOOH) along with siderite ($FeCO_3$) in corrosion products.

ACKNOWLEDGEMENTS

The authors greatly appreciate the following: Cody Shafer for providing the images of the instrumentation involved in this research; The Ministry of Higher Education Malaysia and Universiti Teknologi MARA Malaysia for providing the funds needed for this research; and Ohio University's Russ College of Engineering and Technology for its facilities.

REFERENCES

1. M. B. Kermani and A. Morshed, "Carbon dioxide corrosion in oil and gas production - A compendium," *Corrosion,* 59 (2003): p.659-683.

2. V. White, L. Torrente-Murciano, D. Sturgeon and D. Chadwick, "Purification of oxyfuel-derived CO_2," *Energy Procedia,* 1 (2009): p.399-406.

3. D. A. Jones, *Principles and Prevention of Corrosion,* 2nd ed. (Upper Saddle River, NJ: Prentice Hall, 1996), .

4. H. H. Uhlig, H. H. Triadis and M. Stern, "Effect of oxygen, chlorides, and calcium ion on corrosion inhibition of iron by polyphosphates," *J. Electrochem. Soc.,* 102 (1955): p.59-66.

5. T. Oosterkamp and J. Ramsen, , 2007*"State of the art reviews of CO_2 pipeline transportation with relevance to offshore pipelines"* , Polytec, Norway.

6. B. M. Sass, H. Farzan, R. Prabhakar, J. Gerst, J. Sminchak, M. Bhargava, B. Nestleroth and J. Figueroa, "Considerations for treating impurities in oxy-combustion flue gas prior to sequestration," *Energy Procedia,* 1 (2009): p.535-542.

7. P. N. Seevam, J. M. Race, M. J. Downie and P. Hopkins, "Transporting the next generation of CO_2 for carbon, capture and storage: The impact of impurities on supercritical CO_2 pipelines," *ASME Conf. Proc.,* 2008 (2008): p.39-51.

8. F. Yang, G. Zhao, H. Adidharma, B. Towler and M. Radosz, "Effect of Oxygen on Minimum Miscibility Pressure in Carbon Dioxide Flooding," *Ind Eng Chem Res,* 46 (2007): p.1396-1401.

9. A. T. Laudate. "The JEOL Institute Scanning Electron Microscope Operations Course," Feb 11-14, 2008, JEOL USA Inc, Peabody, MA, 2008.

10. Sonja Richter. "Advanced Use of the SEM," A seminar, April 15, 2013, Institute for Corrosion and Multiphase Technology, Ohio University, Athens, OH, 2013.

11. T. L. Gerke, J. B. Maynard, M. R. Schock and D. L. Lytle, "Physiochemical characterization of five iron tubercles from a single drinking water distribution system: Possible new insights on their formation and growth," *Corros. Sci.,* 50 (2008): p.2030-2039.

12. R. I. Ray, J. S. Lee, B. J. Little and T. Gerke, "The anatomy of tubercles: A corrosion study in a fresh water estuary," *Materials and Corrosion,* 61 (2010): p.993-999.

13. H.M. Herro,"MIC myths - Does pitting cause MIC?" CORROSION/98, Paper No. 278 (Houston, TX: NACE, 1998).

14. P. Sarin, V. L. Snoeyink, J. Bebee, W. M. Kriven and J. A. Clement, "Physico-chemical characteristics of corrosion scales in old iron pipes," *Water Res.,* 35 (2001): p.2961-2969.

15. J. R. Baylis, "Factors other than dissolved oxygen influencing the corrosion of iron pipes," *Industrial & Engineering Chemistry,* 18 (1926): p.370-380.

16. P. Sarin, V. Snoeyink, D. Lytle and W. Kriven, "Iron corrosion scales: model for scale growth, iron release, and colored water formation," *J. Environ. Eng.,* 130 (2004): p.364-373.